Electronic Supplementary Information

Optimizing Electronic Synergy of Atomically Dispersed Dual-Metal Ni-N$_4$ and Fe-N$_4$ Sites with Adjacent Fe Nanoclusters for High-efficiency Oxygen Electrocatalysis

Haibing Meng[‡],[*a], Bin Wu[‡],[*b], Dantong Zhang[‡c], Xuhai Zhu[d], Songzhu Luo[e], Ya You[f], Kai Chen[g], Juncai Long[f], Jiexin Zhu[f], Liping Liu[h], Shibo Xi[i], Tristan Petit[b], Dingsheng Wang[h], Xian-Ming Zhang[*a], Zhichuan J. Xue[e], Liqiang Mai[*f]

[a.]   *College of Chemistry, Taiyuan University of Technology, Taiyuan 030024, P. R. China.*
  E-mail: menghaibing@tyut.edu.cn; zhangxianming@tyut.edu.cn

[b.]   *Helmholtz-Zentrum Berlin für Materialien und Energie GmbH, Albert-Einstein-Straße 15, Berlin 12489, Germany.*
  E-mail: bin.wu@helmholtz-berlin.de

[c.]   *Multiscale Crystal Materials Research Center, Shenzhen Institute of Advanced Technology, Chinese Academy of Sciences Shenzhen 518055, P. R. China.*

[d.]   *State Key Laboratory of Catalysis, Dalian Institute of Chemical Physics, Chinese Academy of Sciences, Dalian, Liaoning 110623, P. R. China.*

[e.]   *School of Materials Science and Engineering, Nanyang Technological University, 50 Nanyang Avenue, Singapore, 639798 Singapore.*

[f.]   *State Key Laboratory of Advanced Technology for Materials Synthesis and Processing, School of Materials Science and Engineering, Wuhan University of Technology, Wuhan 430070, P. R. China.*
  E-mail: mlq518@whut.edu.cn

[g.]   *National Synchrotron Radiation Laboratory, University of Science and Technology of China, Hefei, 230026, P. R. China.*

[h.]   *Department of Chemistry, Tsinghua University, Beijing 100084, P. R. China.*

[i.]*Institute of Chemical and Engineering Sciences, Agency for Science, Technology and Research, Singapore 627833, Singapore.*

[‡] *These authors contributed equally to this work*

Experimental Procedures

Chemicals and materials

Vulcan carbon (XC-72R) was purchased from Carbot Corporation. NiPc and FePc were brought from Alfa Aesar. Pt/C (20 wt%) was purchased from Johnson-Matthey (USA). Nafion solution D520 (5%) was purchased from Dupont Co. (USA). All the reagents and solvents were commercially available and used without further purification.

The N-C was prepared through pyrolyzing XC-72R under NH_3 atmosphere (flow rate: 100 cc/min) at 800 ℃ for 2 h. NiFe-N-C was prepared as follows. NiPc (2.5 mg), FePc (2.5 mg) and N-C (20 mg) were mixed in 10 ml DMF and sonicated for 30 min to facilitate the dissolution and dispersion. After that, the mixture was degassed and refluxed at 120 ℃ under Ar atmosphere for 12 h. After cooling to room temperature, the mixture was filtrated and washed with fresh DMF and ethanol for 2~3 times, respectively. Lastly, the NiFe-N-C was obtained by pyrolyzing the mixture at 500 ℃ for 3 h under Ar atmosphere. The NiFe-N-C' was obtained by 3M sulfuric acid washing of the NiFe-N-C at 80 ℃ for 6 h. The preparations of Ni-N-C and Fe-N-C were similar to that of NiFe-N-C except that the addition of FePc and NiPc were omitted for Ni-N-C and Fe-N-C, respectively.

Materials characterizations

X-ray diffraction (XRD) data were collected on Bruker-AXS D8-A25 ADVANCE (Cu-$K\alpha$ radiation, λ = 1.54184 Å). The scanning electron microscopy (SEM) images were performed on ZEISS Merlin SEM (Carl Zeiss Microscopy, Munich, Germany). The transmission electron microscopy (TEM) and energy dispersive spectrometer (EDS) data were recorded on Cs-corrected FEI Titan G2 300 kV (FEI Ltd., Hillsboro, U.S.A.) and JEM 2010 (JEOL Ltd., Tokyo, Japan). Raman spectra were obtained by using a micro-Raman system with a 532 nm excitation laser (HORIBA LabRAM HR). In situ Raman spectra were recorded at different potentials during OER process in 0.1M air-saturated KOH solution by using a homemade cell. In situ ATR-FTIR was performed on a Nicolet 6700 spectroscopy with a liquid nitrogen cooled mercury-cadmium-telluride (MCT) detector using a homemade three-electrode electrolyzer in order to trace the signals of the intermediates. The spectrum resolution was 4 cm^{-1} and each spectrum was collected for 16 scans. X-ray photoelectron spectroscopy (XPS) was measured using Thermo Fisher ESCALAB 250Xi. Nitrogen adsorption/desorption isotherms were measured on Quantachrome Autosorb iQ instrument at 77 K and the sample was degassed for 8 h at 373 K. The ^{57}Fe Mössbauer measurement was obtained using a 57Co/Rh-source at room temperature in transmission mode. The values of isomer shift (IS), electric quadrupole splitting (QS), *et al.* were obtained through the least square method. The Fe and Ni L-edge X-ray absorption spectra were recorded at the BL12B beamlines of NSRL (Hefei, China). The X-ray absorption near edge structure (XANES) and the extended X-ray absorption fine structure (EXAFS) tests of Ni and Fe K-edge of the catalysts were carried out at the XAFCA beamline of Singapore Synchrotron Light Source (SSLS) in a transmission mode. The in situ X-ray absorption spectra of NiFe-N-C were recorded during OER/ORR process in 0.1 M Air/O_2-saturated KOH solution by using a homemade cell in a fluorescence mode. The Energy was calibrated with Ni foil and Fe foil references. The Data analysis and simulation were performed by the Athena and Artemis software. Inductively coupled plasma optical emission spectroscopy (ICP-OES) was performed on an Agilent 5110.

Electrochemical measurements

The electrochemical measurements were performed on CHI 760E electrochemical workstation (Chenhua, China) with a typical three-electrode system. The Ag/AgCl (saturated KCl) electrode, platinum (Pt) wire, and rotating ring-disc electrode (RRDE, disk electrode area: 0.1256 cm^2, ring electrode area: 0.1884 cm^2) with glassy carbon disk and platinum ring were used as the reference electrode, counter electrode, and working electrode, respectively. The catalyst ink was obtained by dispersing 5.0 mg catalyst powders in 950 μL of isopropanol and 50 μL of 5 wt.% Nafion solution and sonicating for 1 h. Then 5 μL of ink was cast onto the polished surface of the working electrode (catalyst loading: 0.2 mg cm^{-2}). The preparation of catalyst ink of Pt/C was similar to that of prepared catalyst. Before the electrochemical measurements, the working electrode was activated by subjecting to 50 CV cycles in the potential range of 0.2-1.2 V vs the reversible hydrogen electrode (RHE) for ORR and 1.2-1.8 V vs RHE for OER with a scan rate of 100 mV s^{-1}. Cyclic voltammetry (CV) measurements were performed in N_2 or O_2-satureated 0.1 M KOH solution with a scan rate of 10 mV s^{-1}. Linear sweep voltammetry (LSV) measurements were carried out with a scan rate of 5 mV s^{-1} with different rotation rates and all the LSV tests were presented with iR compensation (95% at 0 V). Durability of catalyst was evaluated by performing different CV cycles in the potential range of 0.6-1.1 V for ORR and 1.4-1.7 V vs RHE for OER at room temperature. The chronoamperometry measurements were carried out with an electrode rotation of 1600 rpm under the potential of 0.6 V vs RHE for ORR and the initial potential at the current density of 10 mA cm^{-2} for OER, respectively. The methanol tolerance tests were performed under the potential of 0.6 V vs RHE with an electrode rotation of 1600 rpm by adding 3 mL of methanol into 60 mL O_2-satureated 0.1 M KOH solution. The electrochemical active surface area (ECSA) was determined by measuring the CV curves at different scan rates (20, 40, 60, 80, and 100 mV s^{-1}) and estimated by double-layer capacitance (C_{dl}), which can be evaluated

from the slope of the linear curves between current density differences ($\Delta j = j_a - j_c$ at the potential of 1.03 V vs RHE) versus the scan rates. Electrochemical impedance spectra (EIS) were performed under the frequency of 10^5 -10^{-3} Hz with 5 mV voltage amplitude, and the bias potential is 0.58 V vs RHE. In situ EIS characterization was performed at different potentials during OER/ORR process to disclose the structural information of catalysts and the ion adsorption resistance (R_{ct}) was obtained from equivalent circuit analysis. All the potentials were converted to the RHE according to the following equation:

$$E_{RHE} = E_{Ag/AgCl} + 0.197 + 0.059 pH$$

The electron transfer number (n) and yield of peroxide can be evaluated from the LSV curve of RRDE measurement at 1600 rpm according to the following equation:

$$n = 4\frac{I_D}{I_D + I_R/N}$$

$$H_2O_2(\%) = 200\frac{I_R/N}{I_D + (I_R/N)}$$

where I_D represents disk current and I_R represents ring current at 1.23 V vs RHE. N = 0.37 is the current collection efficiency of the ring electrode.[1]

The Tafel slope was calculated according to the following equation:

$$E = a + b\ log(J_K)$$

$$J_k = \frac{J \times J_L}{J_L - J}$$

where E represents the potential of LSV curve. a is the intercept and b is the Tafel slope. J_k, J and J_L represent kinetic current density, net current density (measured), and diffusion limited current density, respectively.

The electron transfer number (n) and ORR kinetics were evaluated by analyzing LSV curves with rotation rates of 400, 625, 900, 1225, 1600, 2025, and 2500 rpm using the Koutecky-Levich (K-L) equation:

$$\frac{1}{J} = \frac{1}{J_L} + \frac{1}{J_K} = \frac{1}{B\omega^{1/2}} + \frac{1}{J_K}$$

$$\text{with } B = 0.62nFC_0(D_0)^{2/3}v^{-1/6}$$

where ω represents the rotation speed (rad s^{-1}), while F, C_0, D_0 and v are the Faraday constant (96485 C mol^{-1}), concentration of O$_2$ (1.2 × 10^{-6} mol cm^{-3} in O$_2$-saturated 0.1 M KOH), O$_2$ diffusion coefficient (1.9 × 10^{-5} cm^2 s^{-1}) and kinematic viscosity of the solution (0.01 cm^2 s^{-1}).[36]

Zn-air battery measurements

The performance of Zn-air battery was investigated on a LAND-CT2001A testing device. The Zn-air battery was assembled using a polished Zn plate, a catalyst ink-modified gas diffusion electrode (hydrophobic carbon paper) and a 6 M KOH + 0.2 M Zn(Ac)$_2$ solution as electrolyte. The catalyst ink was prepared following the same procedure as described above. The catalyst content on carbon paper was 1 mg cm^{-2}. For Pt/C+IrO$_2$, their respective content on carbon paper was 0.5 mg cm^{-2} (the total catalysts loading: 1 mg cm^{-2}). The open circuit potential, charge and discharge polarization curves were performed on CHI760E electrochemical workstation (the scan rate was 5 mV s^{-1} for polarization curves). The specific capacities of Zn-air batteries were performed at 10 mA cm^{-2} with long time discharge. The galvanostatic cycling stabilities were conducted at the current densities of 10 mA cm^{-2} and 20 mA cm^{-2} with 5 min discharge and 5 min charge time for each cycle.

Computational methods

All DFT calculations were performed using Vienna ab initio simulation package with projector augmented wave (PAW) pseudopotentials. The Perdew-Burke-Ernzerhof (PBE) exchange-correlation functional was used, and cutoff energy for the plane-wave basis set was set to 500 eV. The k-point sampling was obtained from the Monkhorst-Pack scheme with a 3 ×3 × 1 mesh. The convergence criteria of energy and forces were set to 1 × 10^{-5} eV and 0.03 eV Å^{-1}, respectively. The vacuum layer was set at 15 Å to avoid the layer interaction.

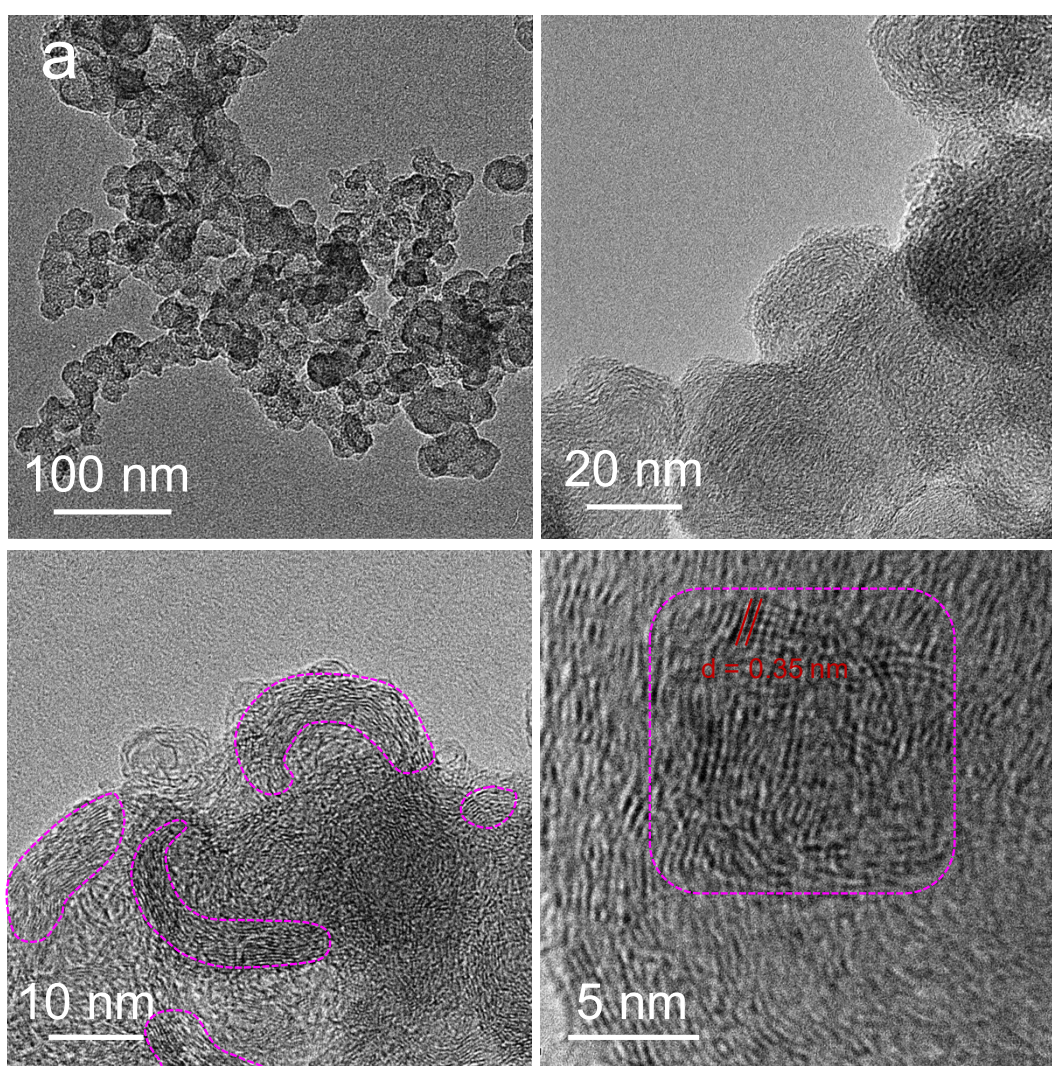The Gibbs free energy can be expressed as

$$\Delta G = \Delta E + \Delta ZPE - T\Delta S$$

where ΔE, ΔZPE, and ΔS are the reaction energy calculated by the DFT methods, the changes in zero-point energies, and the entropy during the reaction, respectively. T is the temperature (298.15 K).
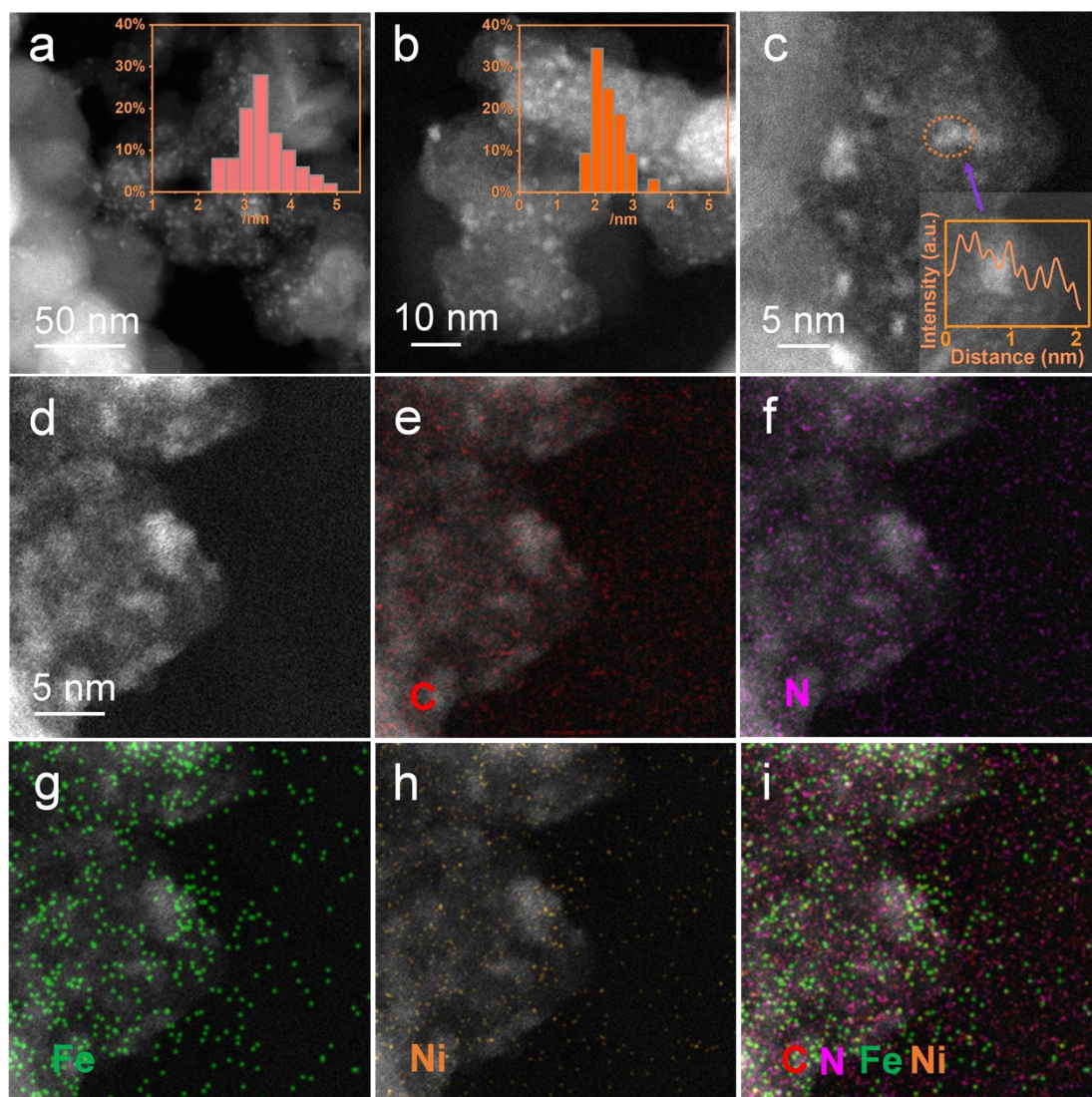
**Supplementary Figures and Tables**
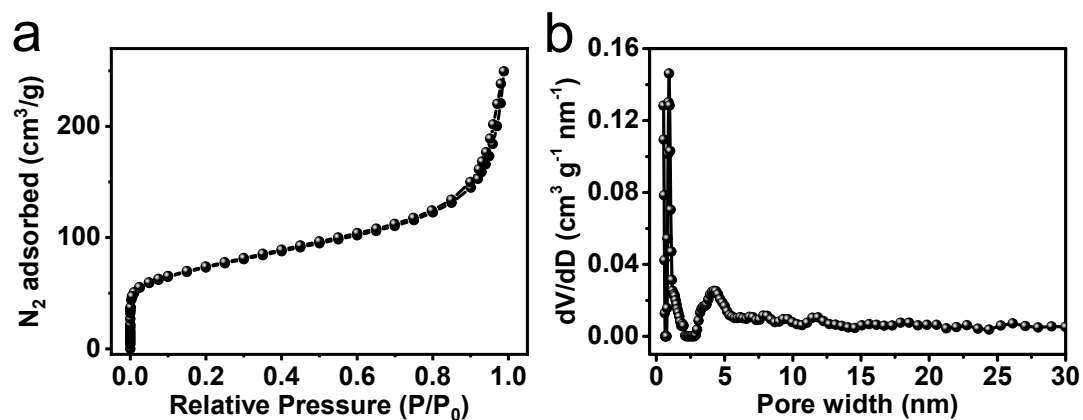
Figure S1. N_2 adsorption/desorption isotherms (a) and pore size distribution (b) of N-C.


Figure S2. TEM and HRTEM images (a-d) of NiFe-N-C. The pink circles indicate the existence of crystalline carbon layers and the interplanar spacing of carbon is 0.35 nm.

Figure S3. (a-c) HAADF-STEM image of NiFe-N-C. Insets in Figure S3a and S3b disclose the size distribution of the Fe nanoclusters. Inset in Figure S3c discloses the interplanar spacing of the Fe nanoclusters. (d) HAADF-STEM images of NiFe-N-C and corresponding EDS elemental mapping of C (e), N (f), Fe (g) and Ni (h) and overlaid C, N, Fe and Ni (i).
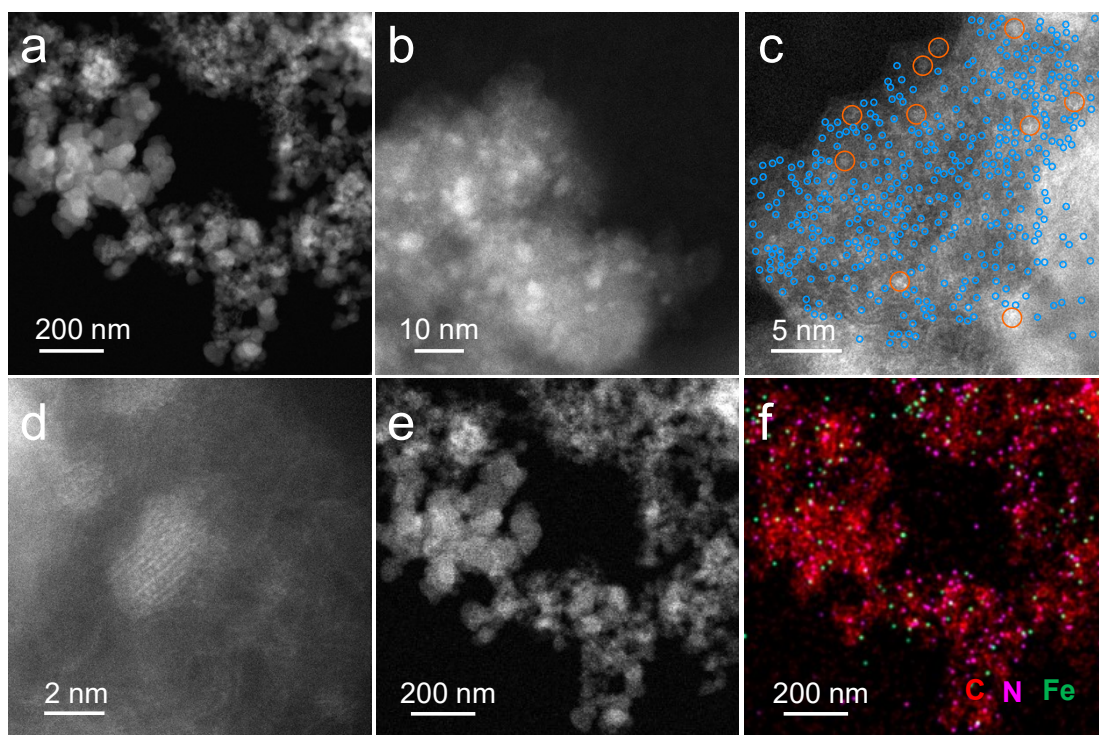
Figure S4. (a-d) HAADF-STEM images of Fe-N-C. (e) HAADF-STEM image of Fe-N-C and (f) corresponding EDS elemental mapping of carbon, nitrogen, and iron.
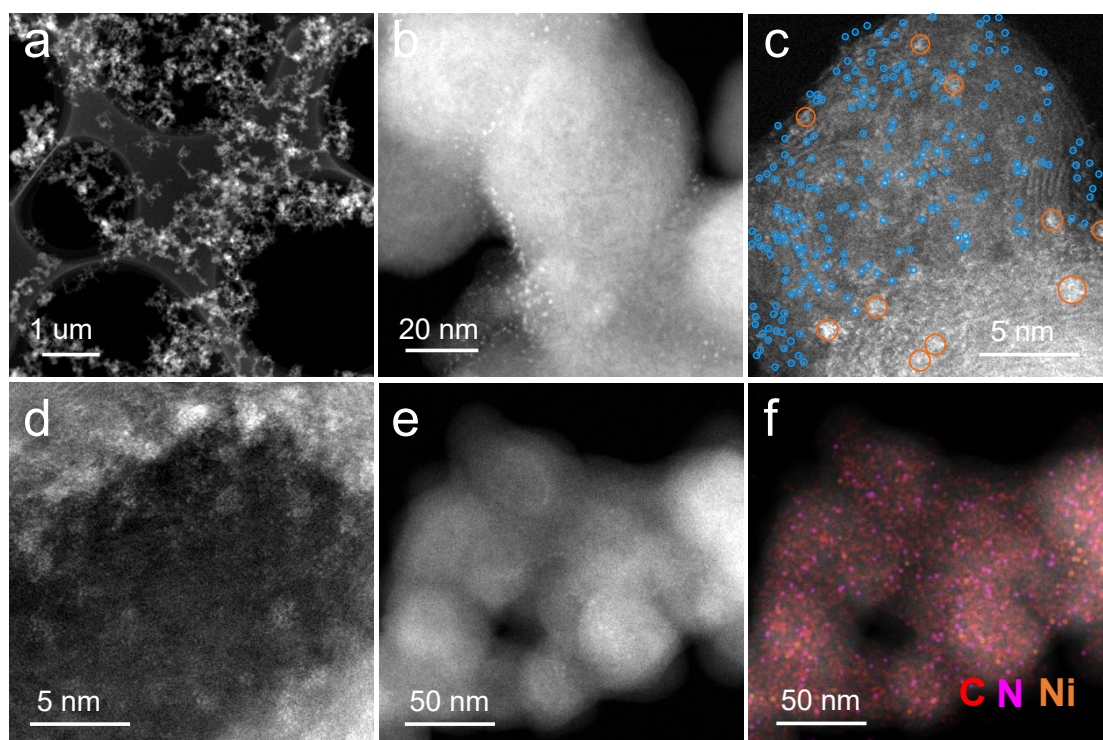

Figure S5. (a-d) HAADF-STEM images of Ni-N-C. (e) HAADF-STEM image of Ni-N-C and (f) corresponding EDS elemental mapping of carbon, nitrogen, and nickel.
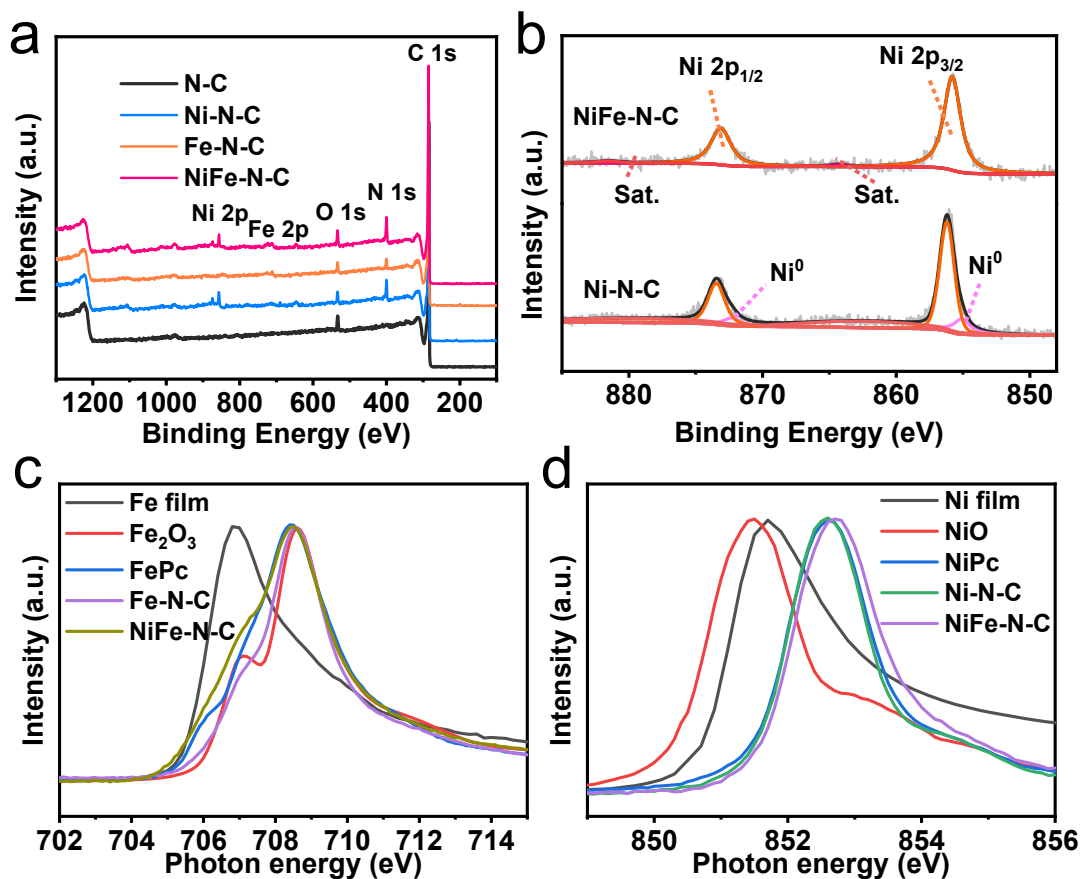
Figure S6. (a) XPS surveys of N-C, Ni-N-C, Fe-N-C and NiFe-N-C. (b) Ni 2p XPS spectra of Fe-N-C and NiFe-N-C. (c) Fe L$_3$-edge XAS spectra of Fe film, Fe$_2$O$_3$, FePc, Fe-N-C and NiFe-N-C. (d) Ni L$_3$-edge XAS spectra of Ni film, NiO, NiPc, Ni-N-C and NiFe-N-C.
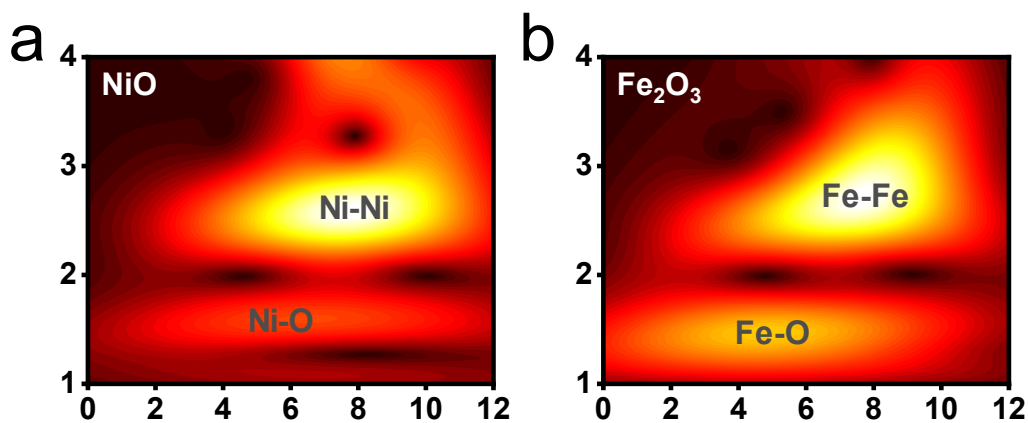
Figure S7. Wavelet transform of the k^3-weighted EXAFS data of Ni K-edge for NiO (a) and Fe K-edge for Fe$_2$O$_3$ (b).
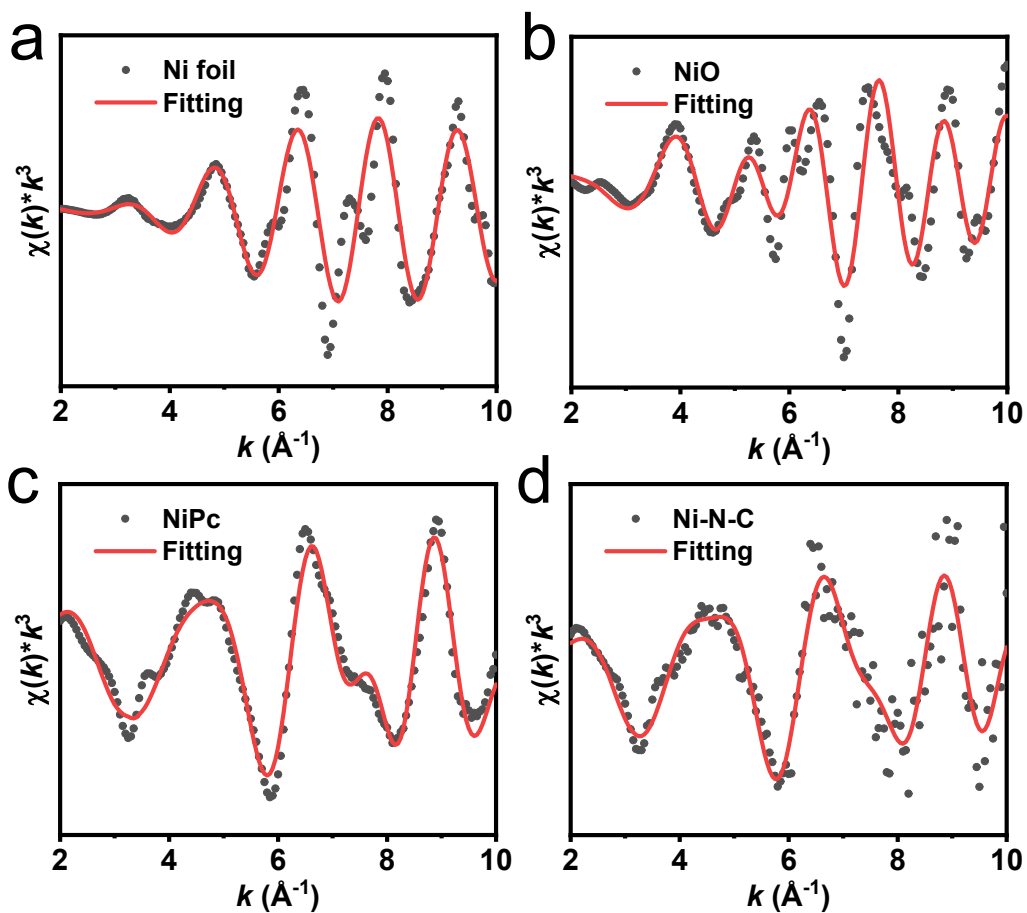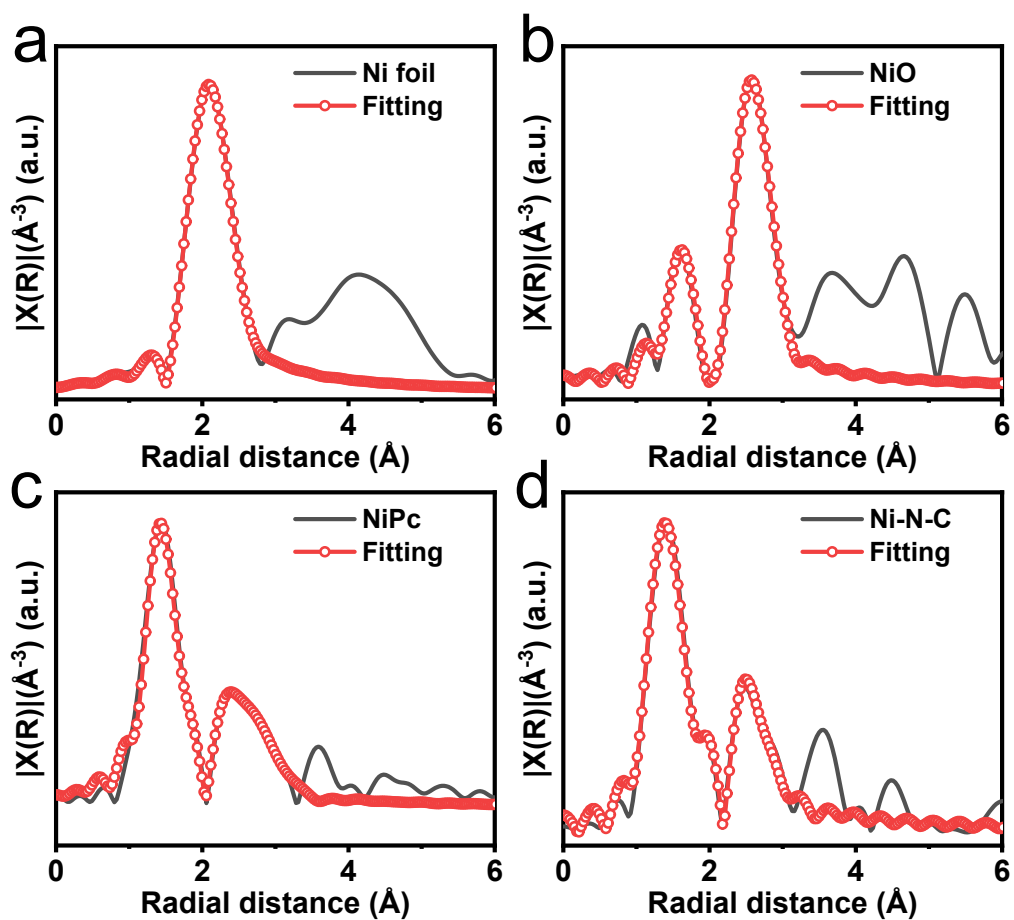
Figure S8. Experimental and fitting FT-EXAFS of Ni K-edge for Ni foil (a), NiO (b), NiPc (c) and Ni-N-C (d) at k space.
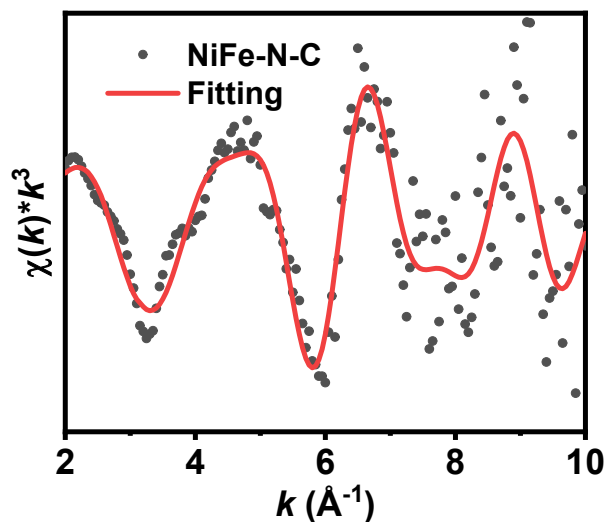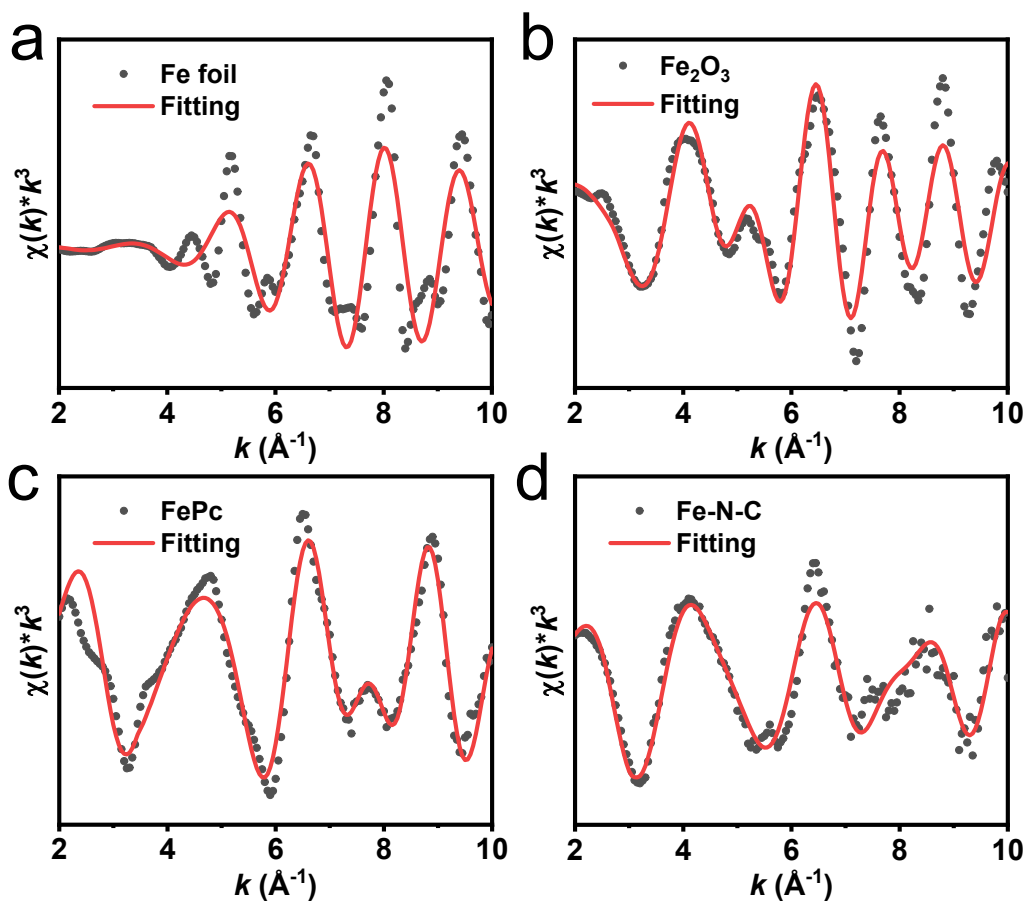

Figure S9. Experimental and fitting FT-EXAFS curves of Ni K-edge for NiFe-N-C at k space.
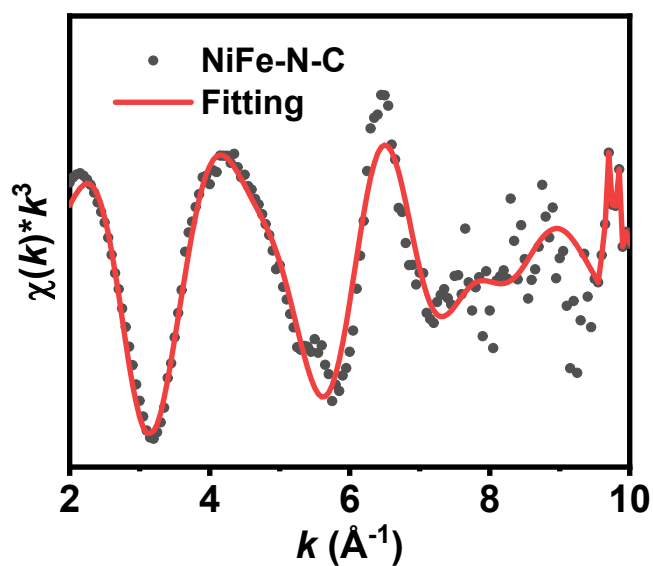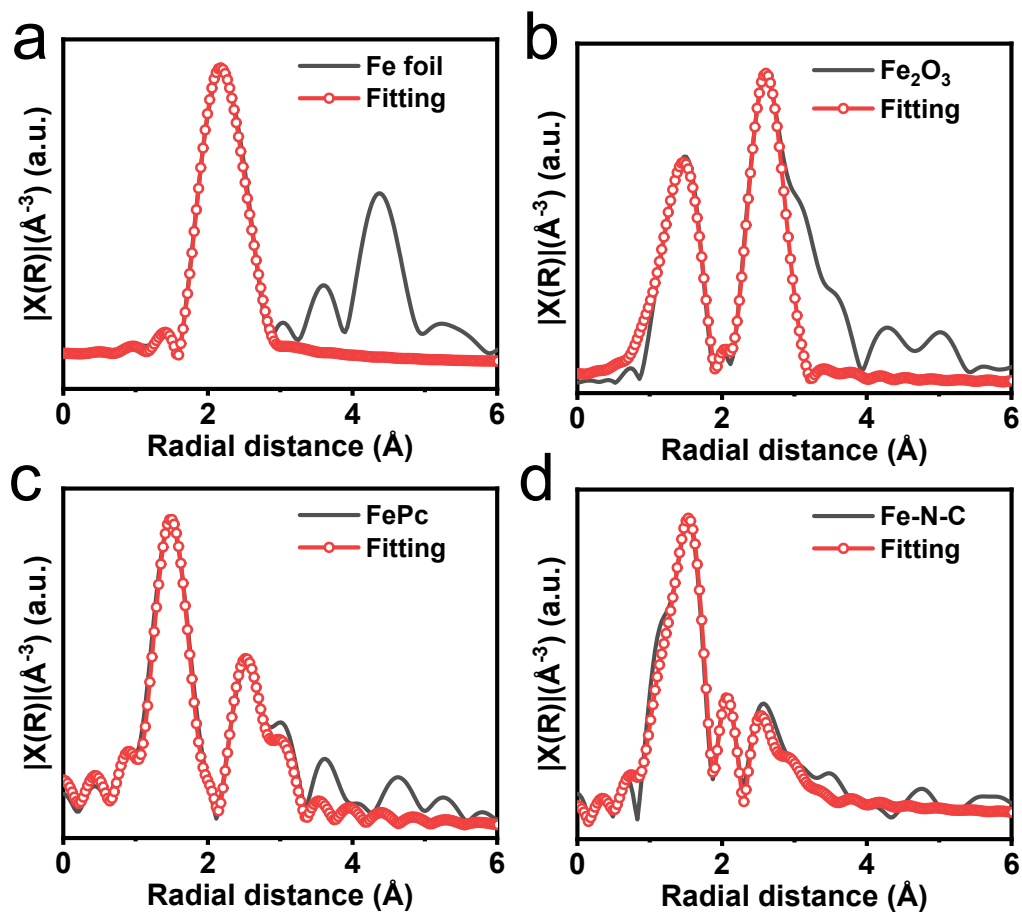
Figure S10. Experimental and fitting FT-EXAFS curves of Ni K-edge for Ni foil (a), NiO (b), NiPc (c) and Ni-N-C (d) at R space.
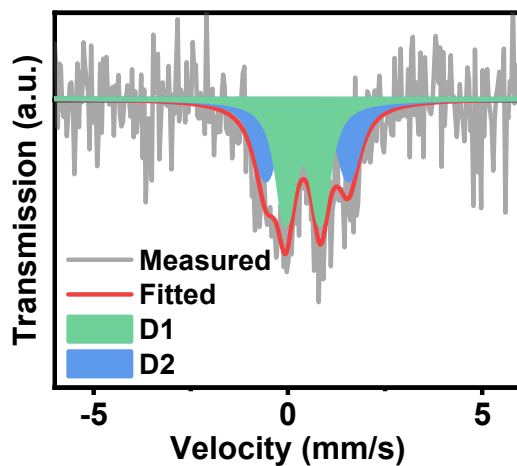
Figure S11. Experimental and fitting FT-EXAFS curves of Fe K-edge for Fe foil (a), Fe_2O_3 (b), FePc (c) and Fe-N-C (d) at k space.
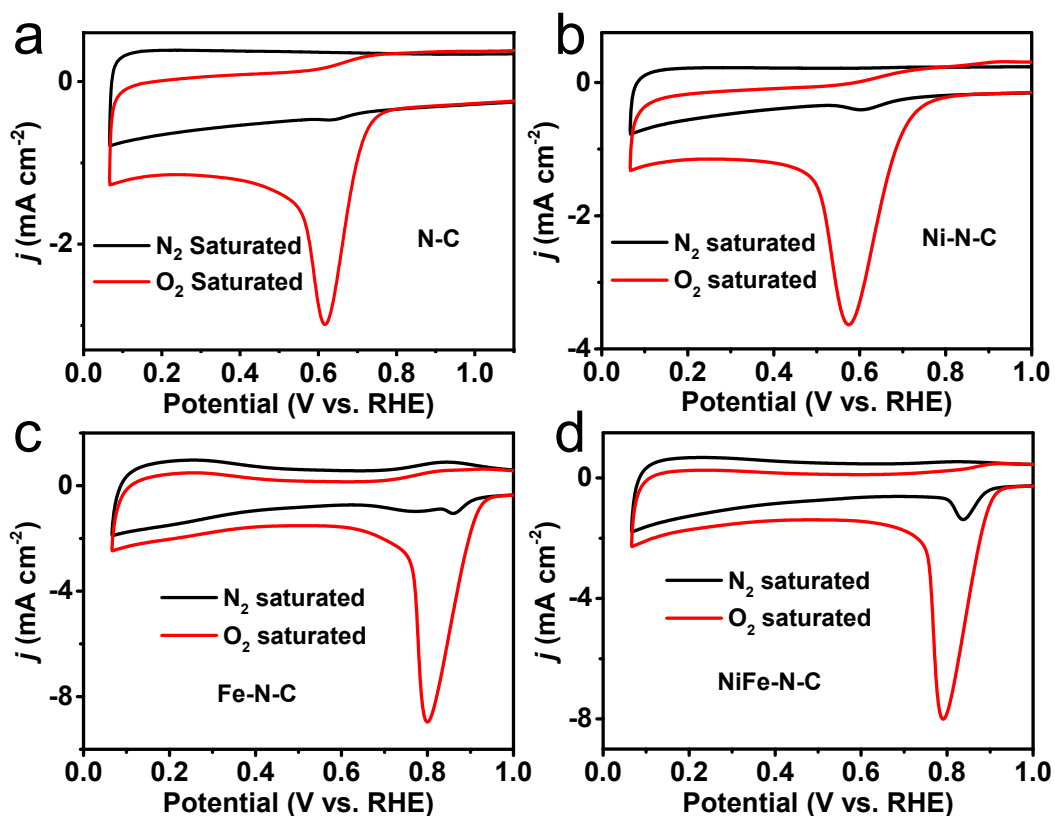

Figure S12. FT-EXAFS fitting curves of Fe K-edge for NiFe-N-C at k space.

Figure S13. Experimental and fitting FT-EXAFS curves of Fe K-edge for Fe foil (a), Fe_2O_3 (b), FePc (c) and Fe-N-C (d) at R space.

Figure S14. ^{57}Fe Mössbauer spectra of NiFe-N-C.

Figure S15. Cyclic voltammetry curves of N-C (a), Ni-N-C (b), Fe-N-C (c) and NiFe-N-C (d) in N_2/O_2 saturated 0.1 M KOH with a scanning rate of 5 mV s^{-1} at 1600 rpm.
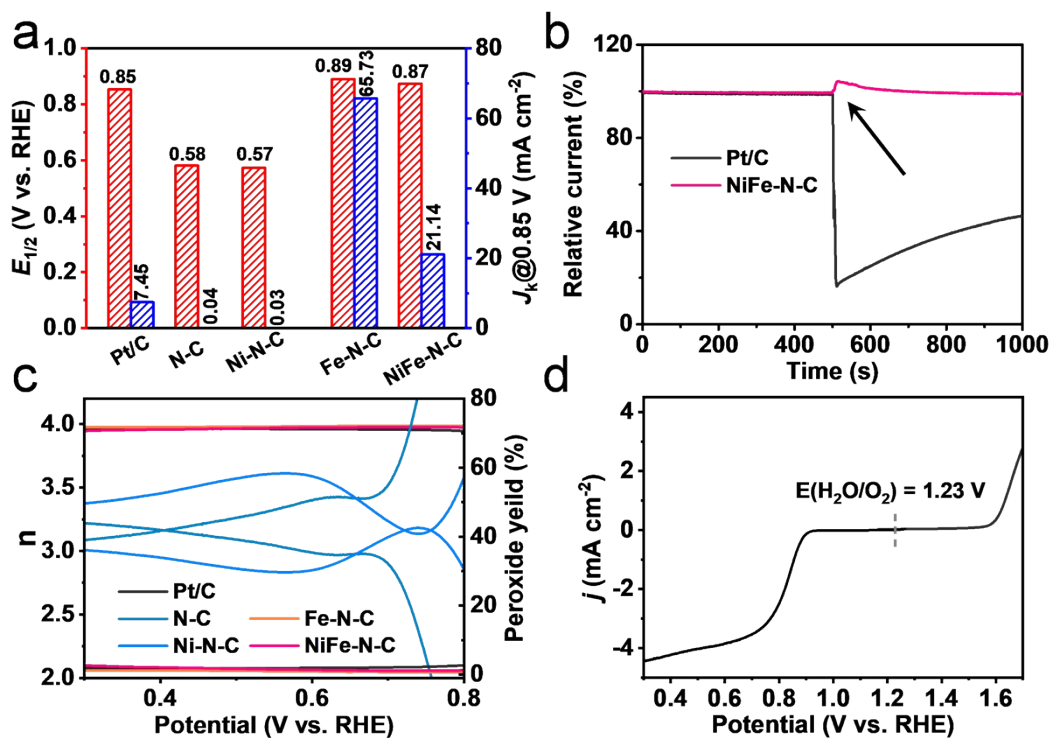
Figure S16. (a) $E_{1/2}$ and J_k at 0.85 V vs RHE for commercial Pt/C and NiFe-N-C. (b) The chronoamperometric plots at 0.6 V vs RHE for commercial Pt/C and NiFe-N-C with a

rotation rate of 1600 rpm. The arrow represents the addition of methanol. (c) Electron transfer number (n) and H_2O_2 yiel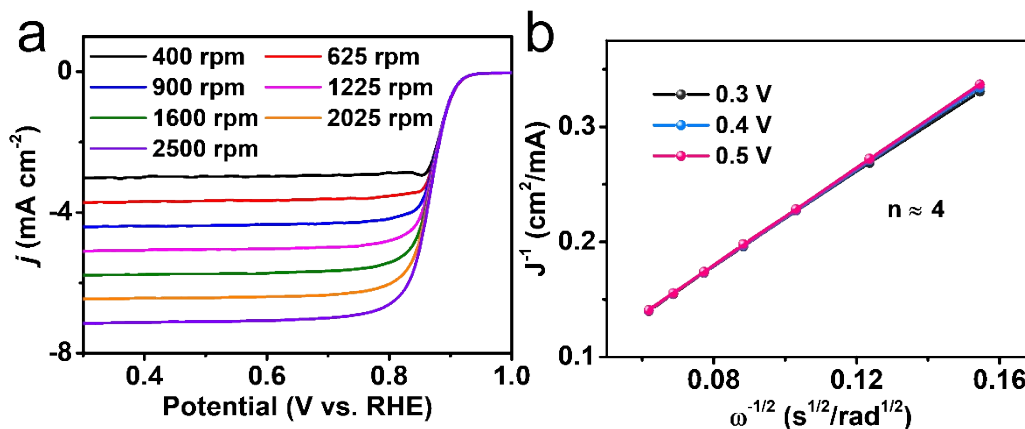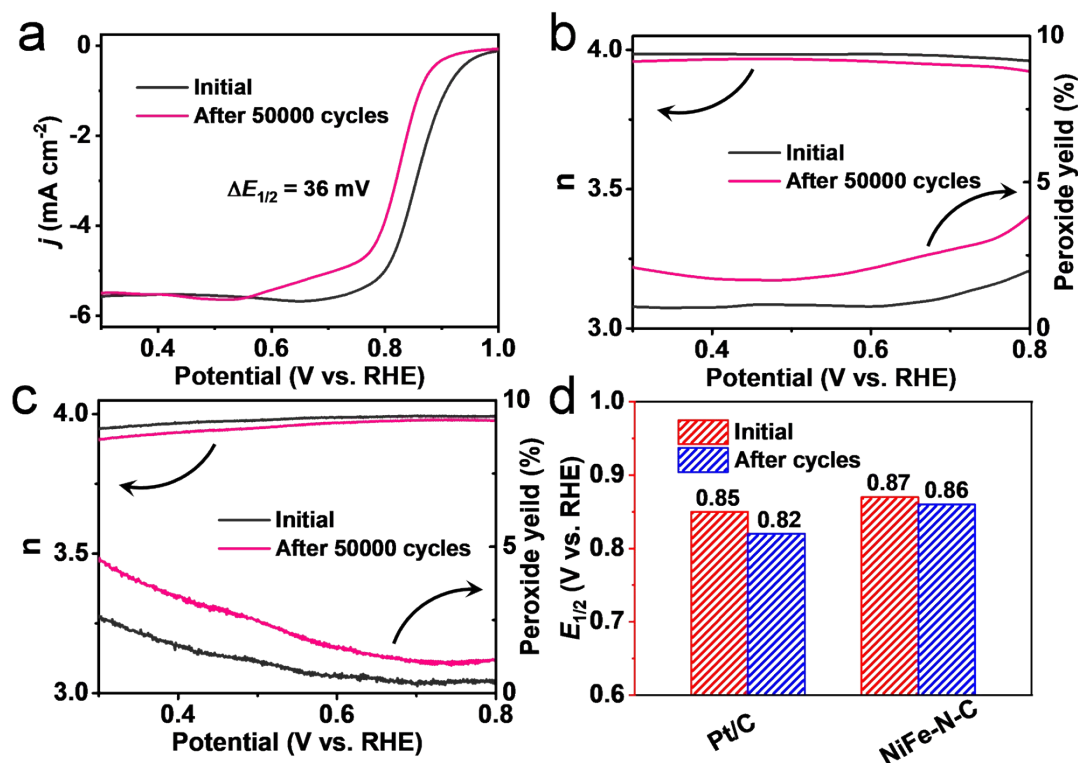ds of Pt/C, N-C, Ni-N-C, Fe-N-C and NiFe-N-C. (d) OER/ORR polarization curves of NiFe-N-C* in 0.1 M air/O_2-saturated KOH with a scanning rate of 5 mV s^{-1} at 1600 rpm.

Figure S17. (a) ORR polarization curves of NiFe-N-C in 0.1 M O_2-saturated KOH with a scanning rate of 5 mV s^{-1} at different rotating speeds and (b) corresponding Koutecky-Levich plots at different potentials.

Figure S18. (a) ORR polarization curves of commercial Pt/C before and after 50000 potential cycles in 0.1 M O_2-saturated KOH with a scanning rate of 5 mV s^{-1} at 1600 rpm. (b) Electron transfer number (n) and H_2O_2 yields of commercial Pt/C before and after 50000

potential cycles. (c) Electron transfer number (n) and H_2O_2 yields of commercial NiFe-N-C

before and after 50000 potential cycles. (d) The changes of $E_{1/2}$ for commercial Pt/C and

NiFe-N-C before and after 50000 potential cycles.
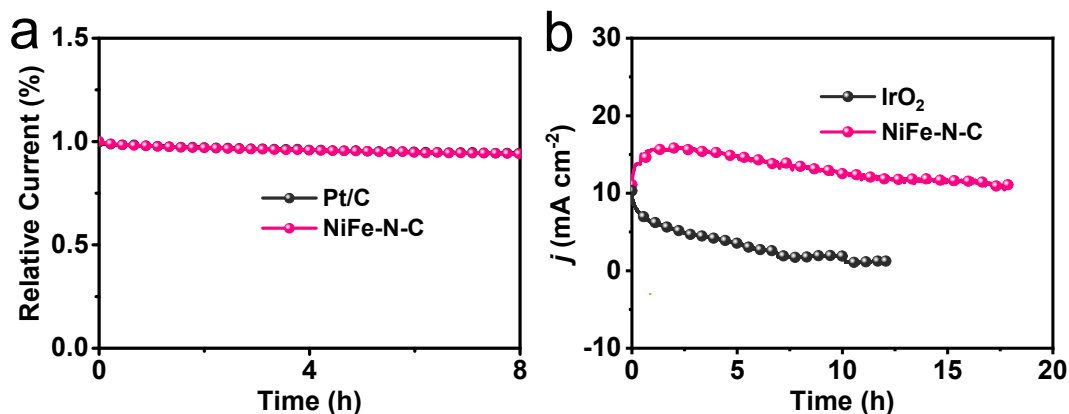
Figure S19. (a) Chronoamperometric curves of commercial Pt/C and NiFe-N-C at 0.6 V vs

RHE for ORR in 0.1 M O_2-saturated KOH with an electrode rotation of 1600 rpm. (b)

Chronoamperometric curves of commercial Pt/C and NiFe-N-C for OER in 0.1 M air-

saturated KOH with an electrode rotation of 1600 rpm.
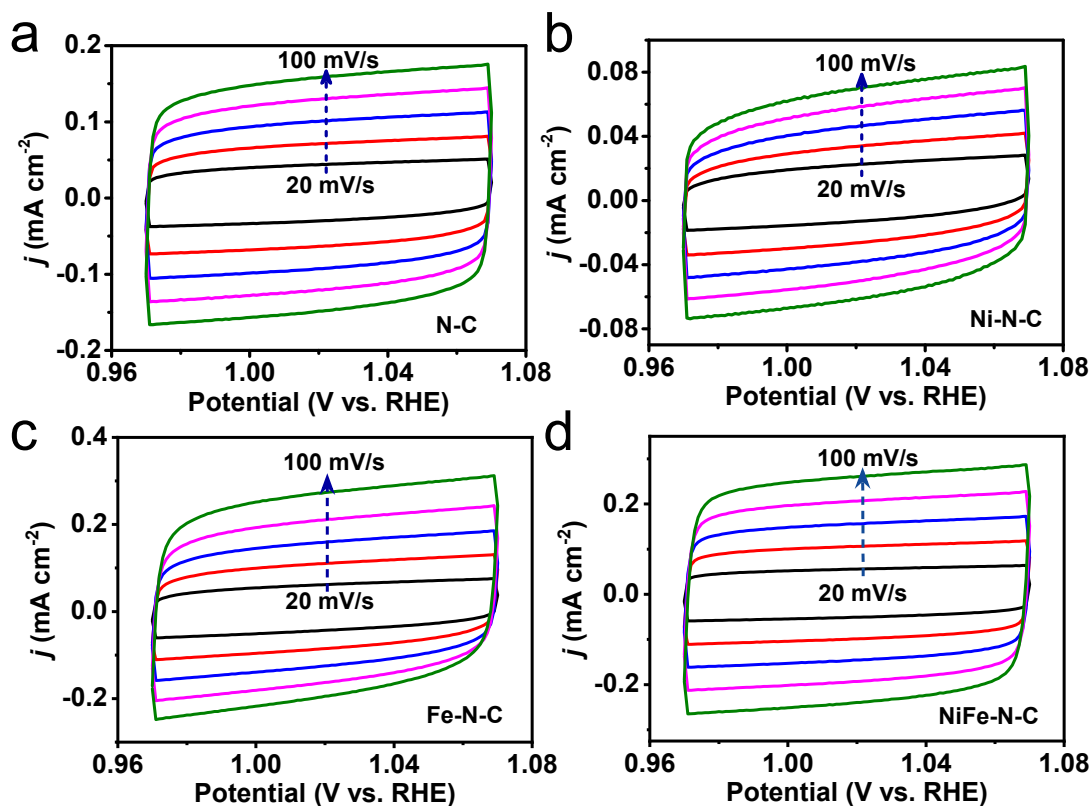
Figure S20. Cyclic voltammograms of N-C (a), Ni-N-C (b), Fe-N-C (c) and NiFe-N-C (d) at

different scan rates in the region of 0.97~1.07 V vs RHE in 0.1 M air-saturated KOH.
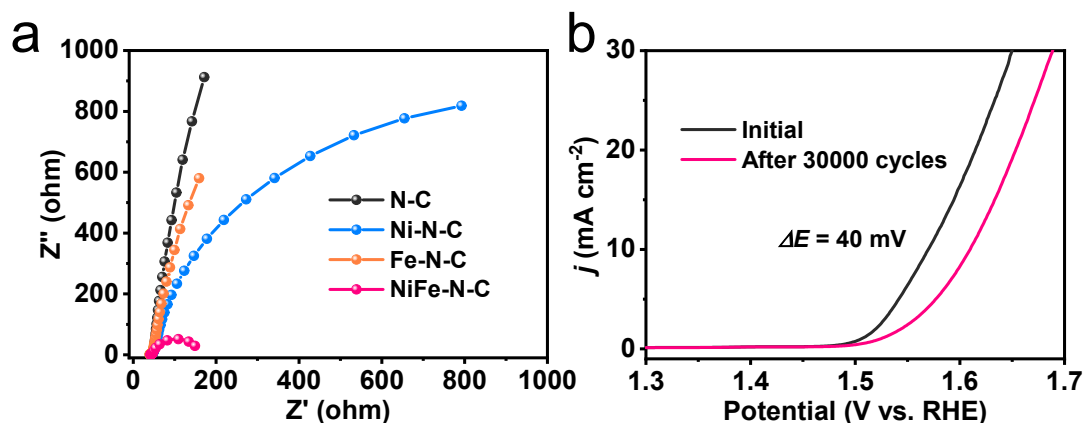
Figure S21. (a) Electrochemical impedance spectra (EIS) of N-C, Ni-N-C, Fe-N-C and NiFe-N-C at the potential of 0.58 V vs RHE. (b) OER polarization curves of commercial IrO_2 before and after 30000 potential cycles between 1.47 and 1.67 V in 0.1 M air-saturated KOH with an electrode rotation of 1600 rpm, ΔE=40 mV was determined at the current density of 10 mA cm^{-2}.
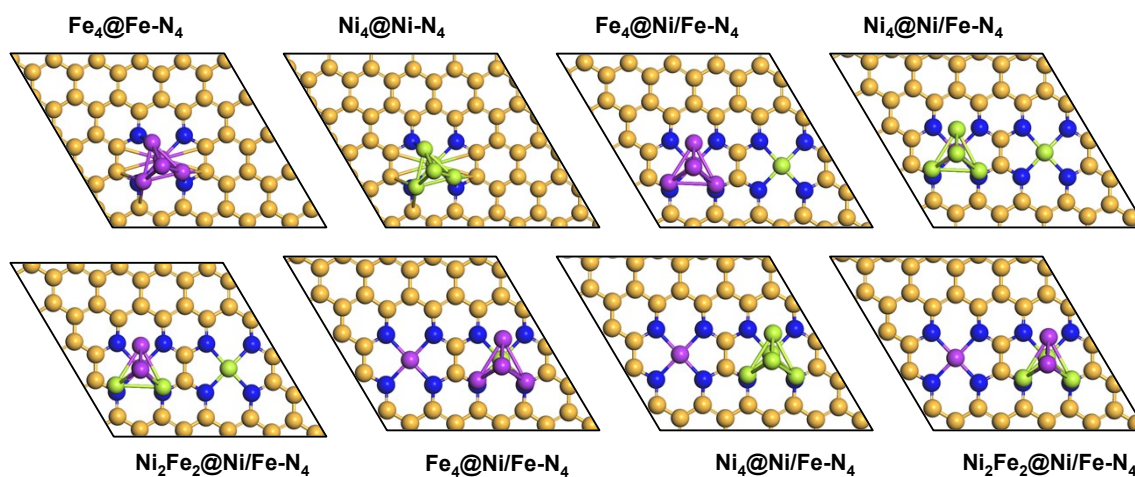
Figure S22. Atomic models of Fe_4@Fe-N_4 (Fe_4 on Fe-N_4 site), Ni_4@Ni-N_4 (Ni_4 on Ni-N_4 site), Fe_4@Ni/Fe-N_4 (Fe_4 on Fe-N_4 site and Ni-N_4 site respectively), Ni_4@Ni/Fe-N_4 (Ni_4 on Fe-N_4 site and Ni-N_4 site respectively), Ni_2Fe_2@Ni/Fe-N_4 (Ni_2Fe_2 on Fe-N_4 site and Ni-N_4 site respectively) systems.
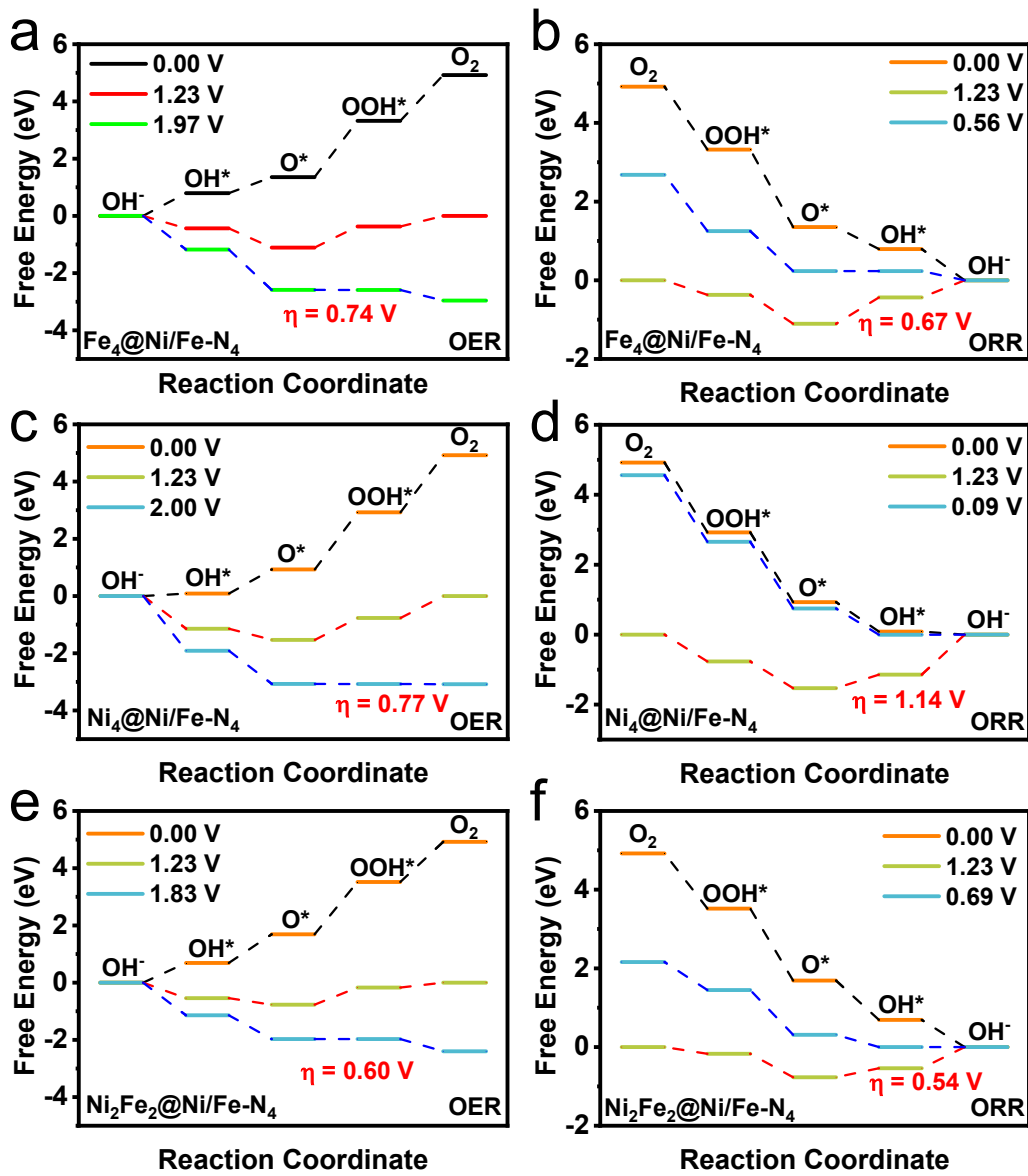
Figure S23. Gibbs free energy diagrams of OER on (a) Fe_4@Ni/Fe-N_4, (c) Ni_4@Ni/Fe-N_4 and (e) Ni_2Fe_2@Ni/Fe-N_4 and ORR on (b) Fe_4@Ni/Fe-N_4, (d) Ni_4@Ni/Fe-N_4 and (f) Ni_2Fe_2@Ni/Fe-N_4. The Fe_4, Ni_4 and Ni_2Fe_4 clusters are assembled on Fe-N_4 site.
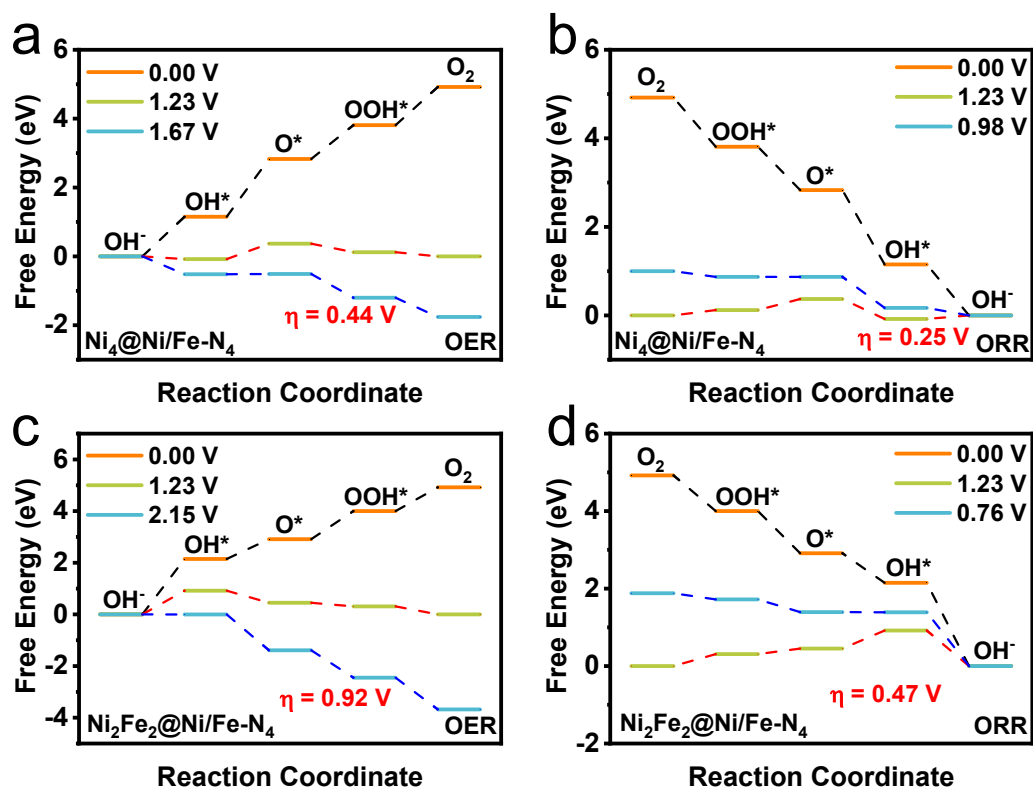
Figure S24. Gibbs free energy diagrams of OER on (a) Ni$_4$@Ni/Fe-N$_4$ and (c) Ni$_2$Fe$_2$@Ni/Fe-N$_4$ and ORR on (b) Ni$_4$@Ni/Fe-N$_4$ and (d) Ni$_2$Fe$_2$@Ni/Fe-N$_4$. The Ni$_4$ and Ni$_2$Fe$_4$ clusters are assembled on Ni-N$_4$ site.
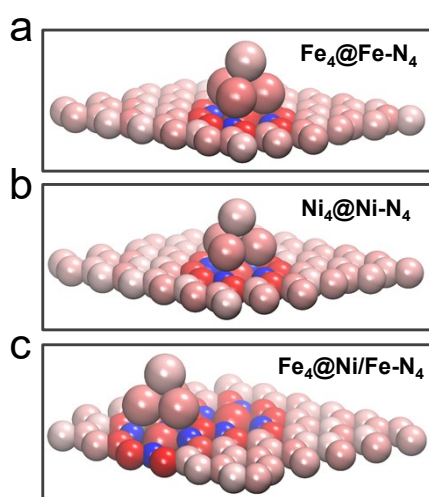
Figure S25. Bader charge of Fe$_4$@Fe-N$_4$ (Fe$_4$ on Fe-N$_4$ site), Ni$_4$@Ni-N$_4$ (Ni$_4$ on Ni-N$_4$ site), and Fe$_4$@Ni/Fe-N$_4$ (Fe$_4$ on Ni-N$_4$ site). Red exhibit the increase of charge number and blue exhibit the decrease of charge number.
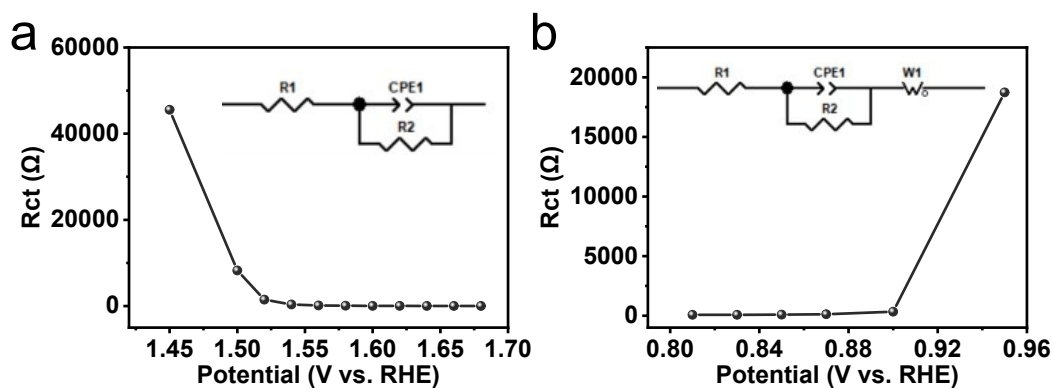
Figure S26. Response of the ion adsorption resistance (Rct) at different potentials for NiFe-N-C electrocatalysts during OER (a) and ORR (b) process. The insets show the accurate equivalent circuits for the charge transfer resistance analysis.
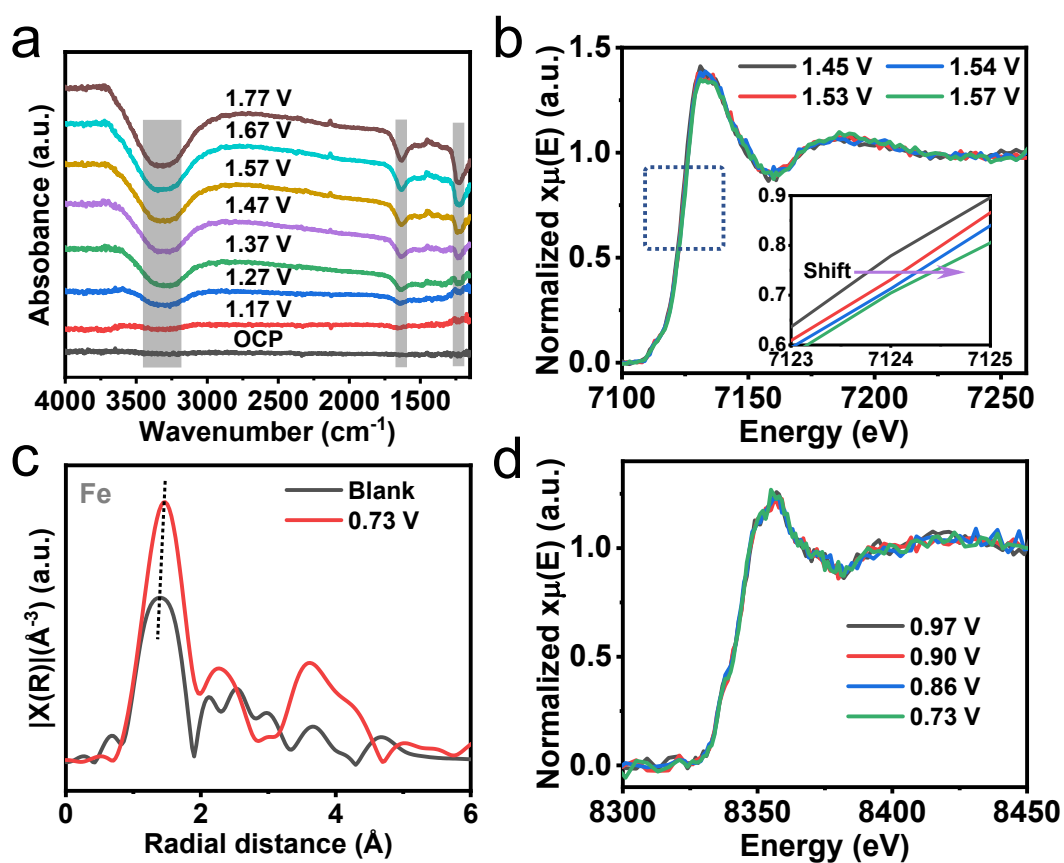
Figure S27. (a) In situ FTIR spectra of NiFe-N-C in 0.1 M O_2-saturated KOH during OER process. (b) In situ Fe K-edge XANES spectra of NiFe-N-C in 0.1 M air-saturated KOH during OER process. (c) Fe K-edge k^3-weighted FT-EXAFS spectra of pristine NiFe-N-C and NiFe-N-C at 0.73 V under ORR condition at R space. (d) In situ Ni K-edge XANES spectra of NiFe-N-C in 0.1 M O_2-saturated KOH during ORR process.
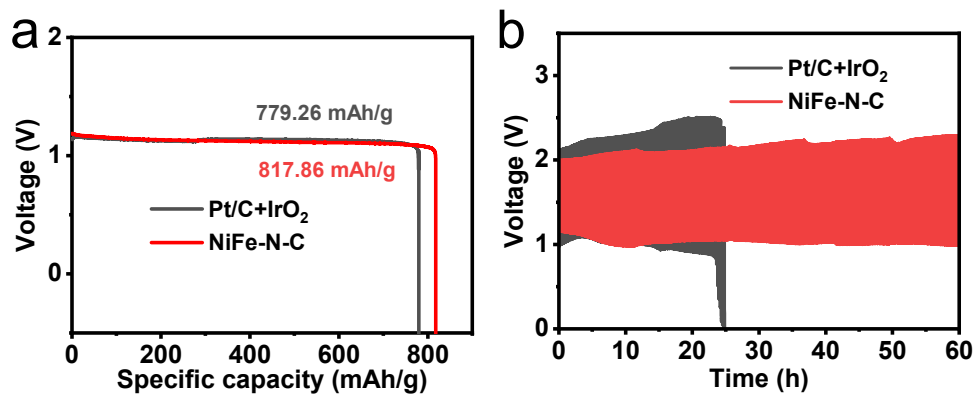
Figure S28. (a) Specific capacities at 10 mA cm^{-2} of NiFe-N-C and Pt/C+IrO$_2$-based Zinc-air batteries. (b) Galvanostatic cycling stabilities of Pt/C+IrO$_2$ and NiFe-N-C based Zinc-air batteries at 20 mA cm^{-2}.

Table S1. The mass ratio of different atoms for Ni-N-C, Fe-N-C and NiFe-N-C based on HAADF-STEM-EDS analysis.

Samples	Ni%	Fe%	C%	N%
Ni-N-C	0.41	NA	97.74	1.85
Fe-N-C	NA	0.73	97.85	1.42
NiFe-N-C	0.85	0.92	94.74	3.49

Table S2. The calculated atomic ratio of different atoms in Ni-N-C, Fe-N-C and NiFe-N-C based on XPS analysis.

Samples	Ni%	Fe%	C%	N%	O%
Ni-N-C	0.71	NA	91.47	5.39	2.02
Fe-N-C	NA	0.65	93.09	3.78	2.48
NiFe-N-C	0.64	0.84	88.22	7.19	3.10

Table S3. Structural parameters at the Ni K-edge extracted from EXAFS fittings (S$_0^2$=0.85).

Sample	Path	CN	R(Å)	σ^2(10^{-3}Å^2)	ΔE$_0$(eV)	R factor
Ni foil	Ni-Ni	12*	2.48	6.15	-4.398	0.0032
NiO	Ni-O	6*	2.08	5.85	1.402	0.0124
	Ni-Ni	12.69	2.95	6.33	-0.747	
NiPc	Ni-N1	4*	1.91	2.65	1.309	0.0103
	Ni-C	8*	2.94	4.90	-0.273	
	Ni-N2	4*	3.28	2.27	0.434	
Ni-N-C	Ni-N	3.50	1.85	2.58	-6.633	0.0161
	Ni-Ni1	1.01	2.33	3.77	-6.633	

	Ni-C	3.55	2.59	3.77	-6.633	
	Ni-Ni2	1.70	2.87	3.77	-6.633	
	Ni-N	4.50	1.89	6.25	-0.897	
	Ni-Fe1	0.50	2.35	6.25	-0.897	
NiFe-N-C	Ni-Fe2	1.17	2.90	6.25	-0.897	0.0118
	Ni-C	1.46	2.92	6.25	-0.897	

S_0^2, CN and R are the amplitude reduction factor, the coordination number and bond length of atoms, respectively. σ^2 represents Debye-Waller factor (a measure of thermal and static disorder in absorber-scatterer distances); ΔE_0 is edge-energy shift (the difference between the zero kinetic energy value of the sample and that of the theoretical model). R factor displays the goodness of the fitting. * This value was fixed during EXAFS fitting. Error bounds of the structural parameters obtained from EXAFS fitting were about CN ± 20%, R ± 1%, σ^2 ± 20% and ΔE_0 ± 20%, respectively.

Table S4. Structural parameters at the Fe K-edge extracted from EXAFS fittings (S_0^2=0.85).

Sample	Path	CN	R(Å)	$\sigma^2(10^{-3}Å^2)$	ΔE_0(eV)	R factor
Fe foil	Fe-Fe	8*	2.47	5.59	-1.063	0.0027
	Fe-Fe	6*	2.84	6.56	-2.836	
Fe_2O_3	Fe-O	5.27	1.98	12.28	-0.282	0.0080
	Fe-Fe	6.08	2.99	9.35	4.129	
FePc	Fe-N1	4*	1.95	4.45	6.490	0.0200
	Fe-C	8*	2.99	3.91	7.966	
	Fe-N2	4*	3.29	6.25	7.966	
Fe-N-C	Fe-N	4.00	1.97	10.03	-1.961	0.0196
	Fe-Fe	0.74	2.43	0.12	-1.961	
	Fe-C1	5.64	2.66	0.12	-1.961	
	Fe-C2	3.85	2.91	0.12	-1.961	
NiFe-N-C	Fe-N	4.00	1.92	10.12	-6.313	0.0227
	Fe-Fe	1.29	2.49	10.12	6.666	
	Fe-C1	6.00	2.60	10.12	-6.313	
	Fe-C2	2.60	3.00	10.12	6.666	

S_0^2, CN and R are the amplitude reduction factor, the coordination number and bond length of atoms, respectively. σ^2 represents Debye-Waller factor (a measure of thermal and static disorder in absorber-scatterer distances); ΔE_0 is edge-energy shift (the difference between the zero kinetic energy value of the sample and that of the theoretical model). R factor displays the goodness of the fitting. * This value was fixed during EXAFS fitting. Error bounds of the structural parameters obtained from EXAFS fitting were about CN ± 20%, R ± 1%, σ^2 ± 20% and ΔE_0 ± 20%, respectively.

Table S5. The Mössbauer parameters and assignments for different Fe species.

Sample	Fe species	IS (mm/s)	QS (mm/s)	LW (mm/s)	Area (%)	Assignment
NiFe-N-C	D1	0.39	0.89	0.70	46.30	$Fe-N_4$, low spin
	D2	0.50	2.13	0.56	53.70	$Fe-N_4$, medium spin

Table S6. Comparison of ORR/OER performance of NiFe-N-C and other reported bifunctional electrocatalysts.

Catalysts	E(V)		ΔE (V)	Tafel slope (mV dec^{-1})		Cyclic Durability		Ref.
	$E_{1/2}$	E_{j10}		ORR	OER	ORR	OER	

NiFe-N-C	0.87	1.55	0.68	33	36	50000	90000	This work
Co-NC@LDH	0.80	1.62	0.82	53.96	79.65	NA	4000	*Chem. Eng. J.* **2020**, 399, 125718
Fe-NiNC-50	0.94	1.68	0.74	55	54	5000	1500	*Nano Energy* **2020**, 71, 104597
Ni,Fe-DSAs/NCs	0.89	1.61	0.72	64	NA	10000	2000	*ACS Nano* **2023**, 17, 8622-8633
Fe_1Co_1-CNF	0.87	1.73	0.86	88	102	NA	1000	*Nano Energy* **2021**, 87, 106147
$FeCoO_x$/N-MWCNTs	0.88	1.61	0.81	NA	NA	NA	NA	*ChemElectroChem* **2021**, 8, 2803
$H_2PO_2^-$/FeNi-LDH-V_2C	0.80	1.48	0.68	52.8	46.5	NA	NA	*Appl. Catal. B: Environ.* **2021**, 297, 120474
IrCo-N-C	0.91	1.56	0.65	54	79	10000	2000	*ACS Catal.* **2021**, 11, 8837-8846
Fe SAs HS	0.86	1.56	0.71	90	68.6	5000	NA	*Angew. Chem. Int. Ed.* **2023**, 62, e202304229
CoO_x@CoN_y/NCNF550	0.78	1.69	0.91	NA	85.6	NA	NA	*ACS Nano* **2021**, 15, 7, 11218–11230
Co SA/NCFs	0.85	1.61	0.76	49.3	NA	50000	NA	*Nano Lett.* **2022**, 22, 2497-2505
Co_9S_8@N, S-C	0.88	1.53	0.65	NA	82.51	10000	10000	*Adv. Energy Mater.* **2021**, 2101249
FeNiSAs/NC	0.84	1.52	0.68	NA	52.68	NA	NA	*Adv. Energy Mater.* **2021**, 11, 2101242
$Ni-N_4$/GHSs/$Fe-N_4$	0.83	1.62	0.79	55	81	NA	NA	*Adv. Mater.* **2020**, 32, 2003134
Pd/FeCo	0.84	1.55	0.71	NA	54	NA	NA	*Adv. Energy Mater.* **2020**, 2002204

meso/micro-FeCo-N$_x$-CN-30	0.89	1.67	0.78	NA	57	NA	NA	*Angew. Chem. Int. Ed.* **2018**, 57, 1856 –1862
A-FeCo@NCNs	0.87	1.67	0.80	98	NA	NA	NA	*J. Catal.* **2021**, 397, 223– 232
3D Co/N-C	0.84	1.56	0.72	51	NA	5000	5000	*Chem. Eng. J.* **2022**, 433, 134500
Ni-NCNT-750	0.88	1.61	0.73	NA	202	NA	NA	*Small* **2020**, 2002518
Fe$_1$Co$_3$-NC-1100	0.88	1.58	0.70	69.06	99.93	NA	5000	*ACS Catal.* **2022**, 12, 1216- 1227
FeNiCo@NC-P	0.84	1.54	0.70	53	64	NA	NA	*Adv. Funct. Mater.* **2019**, 1908167
Co-N$_x$-YSC-600/CC	0.8 (4.67)	1.66 (4.5)	NA	85.3	186.1	NA	NA	*Nano Energy* **2021**, 89, 106314
Co$_1$-PNC/Ni$_1$-PNC	0.88	1.62	0.74	63	117	5000	NA	*Nano Res.* **2021**, 14(10): 3482–3488
RuFe@NC-900(5h)	0.86	1.58	0.73	63.2	140	5000	NA	*ACS Catal.* **2022**, 12, 1718- 1731
CoNC SAC	0.86	1.65	0.79	47.9	106.9	NA	NA	*Sci. Adv.* **2022**, 8, eabn5091
Fe/SNCFs-NH$_3$	0.89	1.68	0.79	70.82	NA	6000	NA	*Adv. Mater.* **2021**, 2105410
S-CFZ	0.85	1.53	0.68	79	NA	NA	NA	*J. Am. Chem. Soc.* **2022**, 144, 11, 4783–4791

Table S7. The Nyquist plots fitting results of NiFe-N-C.

	Potential (V)	R_s (Ω)	C_{dl} (F)	R_{ct} (Ω)
	1.45 V	41.71	0.00016051	45536
	1.50 V	40.13	0.00020947	8266
	1.52 V	41.11	0.00021533	1487
OER process	1.54 V	41.65	0.00022117	366.4
	1.56 V	40.47	0.00025406	137.6
	1.58 V	40.43	0.00031138	73.79
	1.60 V	40.39	0.00038268	49.66
	1.62 V	40.48	0.00052345	37.86

	1.64 V	39.65	0.00060902	30.77
	1.66 V	40.27	0.0005587	25.61
	1.68 V	39.80	0.00071074	22.83
	0.95 V	47.96	0.0001608	18733
	0.90 V	45.31	0.00019643	366.1
ORR process	0.87 V	40.19	0.00029126	117.9
	0.85 V	39.46	0.00034421	83.28
	0.83 V	38.66	0.00042797	72.83
	0.81 V	38.39	0.00054161	74.86

Table S8. Comparison of Zn-air performance based on NiFe-N-C and other reported bifunctional electrocatalysts in literature.

Catalysts	Open-circuit voltage (V)	Peak power density (mW cm^{-2})	Specific capacity (mAh g$_{Zn}^{-1}$)	Battery Stability (h)	Ref.
NiFe-N-C	1.59	153	818	700 (10)	This work
Co-NC@LDH	1.41	107.8	806	300 (5)	*Chem. Engin. J.* **2020**, 399, 125718
Fe-NiNC-50	1.41	200	932.66	100 (2)	*Nano Energy* **2020**, 71, 104597
Fe$_1$Co$_1$-CNF	1.45	201.7	814	200 (20)	*Nano Energy* **2021**, 87, 106147
Ni,Fe-DSAs/NCs	1.49	217.5	780.1	500 (5)	*ACS Nano* **2023**, 17, 8622-8633
H$_2$PO$_2^-$/FeNi-LDH-V$_2$C	1.42	137	NA	100 (5)	*Appl. Catal. B: Environ.* **2021**, 297, 120474
IrCo-N-C	1.46	138.8	NA	225 (5)	*ACS Catal.* **2021**, 11, 8837-8846
Co SA/NCFs	1.53	154.5	796	600 (10)	*Nano Lett.* **2022**, 22, 2497-2505
Co$_9$S$_8$@N, S-C	1.51	259	991	110 (10)	*Adv. Energy Mater.* **2021**, 2101249
Fe SAs HS	NA	170	785	65 (20)	*Angew. Chem. Int. Ed.* **2023**, 62, e202304229
FeNi SAs/NC	1.45	42.22	779.4	20 (1)	*Adv. Energy Mater.* **2021**, 11, 2101242
Ni-N$_4$/GHSs/Fe-N$_4$	1.45	NA	970.4	200 (10)	*Adv. Mater.* **2020**, 32, 2003134
Pd/FeCo	1.42	117	854	200 (10)	*Adv. Energy Mater.* **2020**, 2002204
meso/micro-FeCo-N$_x$-CN-30	1.40	150	NA	40 (5)	*Angew. Chem. Int. Ed.* **2018**, 57, 1856 –1862
A-FeCo@NCNs	1.46	132	736.2	167 (2)	*J. Catal.* **2021**, 397, 223–232
3D Co/N-C	NA	239	NA	300 (10)	*Chem. Eng. J.* **2022**, 433, 134500
Ni-NCNT-750	1.48	120	834.1	375 (10)	*Small* **2020**, 2002518
Fe$_1$Co$_3$-NC-1100	1.48	372	NA	190 (10)	*ACS Catal.* **2022**, 12, 1216-1227
FeNiCo@NC-P	1.36	112	NA	120 (10)	*Adv. Funct. Mater.* **2019**, 1908167
Co-N$_x$-YSC-600/CC	1.345	55.3	NA	200 (10)	*Nano Energy* **2021**, 89, 106314
Co$_1$-PNC/Ni$_1$-PNC	1.59	252	874	45 (10)	*Nano Res.* **2021**, 14(10): 3482–3488
RuFe@ NC-900(5h)	1.43	NA	752	30 (10)	*ACS Catal.* **2022**, 12, 1718-1731
CoNC SAC	NA	161.8	795	80 (5)	*Sci. Adv.* **2022**, 8, eabn5091
Fe/SNCFs-NH$_3$	1.38	255.84	NA	1000 (1)	*Adv. Mater.* **2021**, 2105410
S-CFZ	NA	178	NA	525 (25)	*J. Am. Chem. Soc.* **2022**, 144, 11, 4783–4791